Nanoscale

Accepted Manuscript

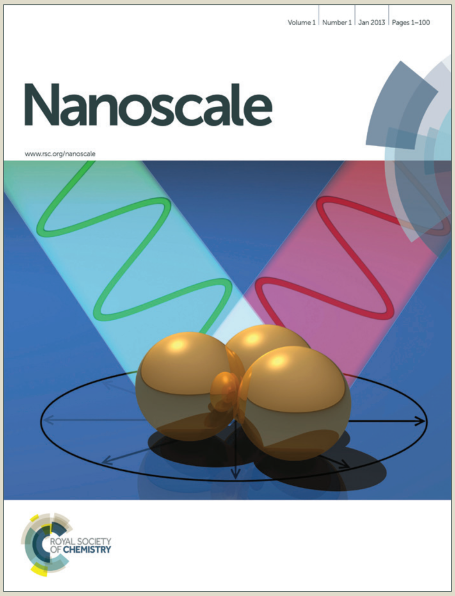

ROYAL SOCIETY OF CHEMISTRY

www.rsc.org/nanoscale

Nanoscale

Dynamic Article Links ►

Cite this: DOI: 10.1039/c0xx00000x

www.rsc.org/xxxxxx

ARTICLE TYPE

Facile Preparation of Ordered Mesoporous $MnCo_2O_4$ for Low-temperature Selective Catalytic Reduction of NO with NH_3

Mingying Qiu[a], Sihui Zhan*[a], Hongbing Yu*[a], Dandan Zhu[a] and Shengqiang Wang [a]

Received (in XXX, XXX) Xth XXXXXXXXX 20XX, Accepted Xth XXXXXXXXX 20XX

DOI: 10.1039/b000000x

Abstract: The ordered mesoporous $MnCo_2O_4$ nanomaterials were successfully prepared through the nanocasting route using SBA-15 and KIT-6 as hard template, respectively. These mesoporous nanomaterials were characterized by XRD, BET, TEM, NH_3-TPD, H_2-TPR, NO-TPD, XPS and DRIFT. The low temperature selective catalytic reduction (SCR) activity of NO with NH_3 was investigated, which revealed that 3D-$MnCo_2O_4$ using KIT-6 as template can totally clean all NO over a wide temperature range of 100-250°C with a gas hourly space velocity (GHSV) of 32,000 h^{-1}, while the 2D-$MnCo_2O_4$ with SBA-15 as template had 95% conversion rate at the same condition. The 3D-$MnCo_2O_4$ showed the best performance to clean NO due to their typical three-dimensional porous structure, large specific surface area, abundant active surface oxygen species and Lewis acid sites. All the results indicate that novel cheap catalyst for catalytic removal of NO can be designed by morphology control at nanoscale.

1. Introduction

Nitrogen oxide (NOx) emitting from combustion of fossil fuels are currently is one of the main pollutants in the atmosphere, its emissions have caused a series of environmental problems, such as photochemical smog, acid rain, city haze weather, and greenhouse effects.[1-4] In the NOx emission control technologies, selective catalytic reduction of NO with NH_3 (NH_3-SCR) has been widely used in coal-fired power plants and other stationary sources NOx eliminate.[5] Vanadium-based catalysts are used worldwide due to the desirable catalytic activity at 300-400°C.[6-9] However, some inevitable drawbacks of this class of catalysts are still serious, such as the toxicity of vanadium, SO_2 oxidation to SO_3, narrow operation temperature window (300-400 °C) and especially the poor activity at low-temperature regions. Therefore, it is a trend of the development of novel low temperature SCR catalysts to replace the traditional catalysts in the future.

On the basis of low cost, environmentally friendly and high catalytic performance at the low temperature NH_3-SCR reaction, MnOx-based catalysts have been the main research object recently. Unfortunately, they are very sensitive to the presence of SO_2 in the exhaust, and the low N_2 selectivity limited the temperature activity and practical application.[10-13]Appropriate combinations of metal oxides can exhibit higher activity and thermal stability than the single oxides. Zhang et al. have reported that MnOx-CeOx can improve the activity, stability and SO_2-tolerance of the catalyst due to the interaction of MnOx and CeO_2.[14] Wan et al. found that the catalytic activity of MnOx have been effectively enhanced by the addition of nickel species due to the synergetic catalytic effect.[15] There are few works addressed to the catalytic properties of combinations of manganese oxides and cobalt oxides in NH_3-SCR reaction, because of the nanoparticles could agglomerate easily during the catalytic process, resulting in the decline of catalytic activity. In addition, it is well established that nano- and microscopic control of the structure, size, and shape of inorganic materials can lead to novel electronic, magnetic, optical, and catalytic properties that are not found in such materials' bulk counterparts.[16-19] Zhang et al. have reported that the hollow porous $MnxCo_{3-x}O_4$ nanocages synthesized via a self-assemble method possess a much better catalytic activity than conventional $MnxCo_{3-x}O_4$ nanoparticles and the main reason is attributed to the hollow and porous structures.[20] Nowadays, ordered mesoporous materials with large surface-to-volume ratios and uniform porous structure are of much interest, because they may present numerous edges and corners for the adsorption and activation of reactants and the pores are benefit to the mass transfer process at the gas-solid phase boundary.[21, 22] Compared to the nanoparticles, mesoporous transition metal oxides are particularly important because they possess d-shell electrons confined to nanosized walls, redox active internal surfaces, and connected pore networks. With these attributes they exhibit many interesting properties in energy conversion and storage, catalysis, sensing, adsorption, separation, and magnetic devices.[23-28] In the past few years, only a few single component metal oxides have been successfully obtained through the nano-casting method, such as Co_3O_4,[29,30] CeO_2[31, 32] and Cr_2O_3.[33] In this paper, a highly ordered mesoporous $MnCo_2O_4$ was synthesized via the nano-casting method, which were characterized by XRD, BET, TEM, NH_3-TPD, H_2-TPR, XPS and DRIFT. As compared with bulk-$MnCo_2O_4$ and mesoporous 2D-$MnCo_2O_4$, mesoporous 3D-

$MnCo_2O_4$ exhibits ultra-high low temperature catalytic activity for cleaning NO with NH_3 from 100 to 250 °C. The mechanism has been studied based on XPS, TPD and DRIFT results.

2. Experimental Section

2.1 Preparation of materials

$Co(NO_3)_2\cdot 6H_2O$ (99%), $Mn(NO_3)_2\cdot 4H_2O$(99%), and Pluronic P123 (M_n= 5800) were purchased from Sigma-Aldrich, 1-butanol (99.4%), HCl(37%), NaOH (99.3%), n-Hexane(98%) and tetraethyl orthosilicate (98%) were purchased from Aladdin Industrial Inc.

The template SBA-15 and KIT-6 was synthesized according to the previous literature, respectively.[34,35] The "bi-solvents" method was adopted to synthesize nanostructured spinel materials. In a typical synthesis process, 1.0 g KIT-6 or SBA-15 was suspended in 70 mL dry n-hexane, then stirred for 3 h, 1.0 mL aqueous solution containing 2.3 mmol $Mn(NO_3)_2\cdot 4H_2O$ and 4.6 mmol $Co(NO_3)_2\cdot 6H_2O$ was added dropwise with vigorous stirring. The mixture was stirred overnight, filtered and dried at 40 °C, then calcined in a muffle furnace at 450 °C for 4 h with a heating rate of 1°C/min. Finally, the sample was treated twice with a hot 2 M NaOH aqueous solution, then centrifuged, washed and dried at 100°C. The products were denoted as 2D-$MnCo_2O_4$ (for the SBA-15 template), 3D-$MnCo_2O_4$ (for the KIT-6 template), respectively. As a comparison, the bulk catalyst $MnCo_2O_4$ was synthesized by the co-precipitation method with the same precursors,[36] which was labeled as B-$MnCo_2O_4$.

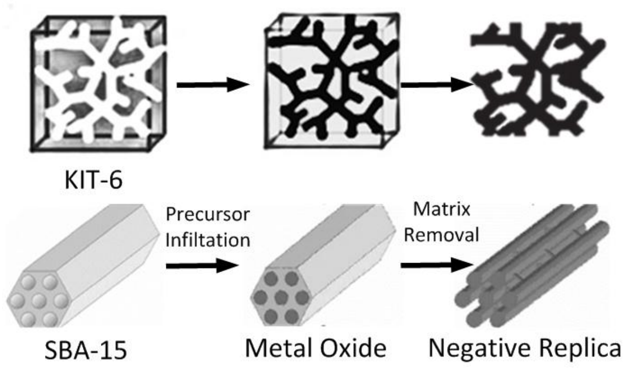

Fig. 1 Schematic representation of the the in situ synthesis process of the mesoporous catalysts with KIT-6and SBA-15

2.2 Characterization

The Powder X-ray diffraction（XRD）patterns were carried out on a Rigaku D/MAX 2500v/PC instrument using Cu Ka radiation (λ=0.15418 nm). The nitrogen adsorption-desorption isotherms was measured using a Quantachrome Autosorb IQ instrument operated at -196°C. Prior to the test, the sample was degassed under vacuum for 4 h at 250°C. The specific surface areas were calculated by the Brunauer-Emmett-Teller (BET) method, the pore size distributions of the samples were calculated using the adsorption branches.[36] TEM studies were carried out by using a JEOL JEM 2100F instrument with an accelerating voltage of 200 kV. Prior to analysis, each sample was dispersed in ethanol by sonication and deposited on a copper grid coated with a carbon film. Temperature programmed reduction by hydrogen (H_2-TPR) was obtained on a Micromeritics Autochem 2920 II instrument with a thermal conductivity detector (TCD). 100 mg of the catalyst was outgassed at 300 °C under a N_2 atmosphere. After cooling to room temperature under a N_2 atmosphere, the flowing gas was switched to 5% H_2/N_2 and the sample was heated to 900 °C at a heating rate of 10 $°C\cdot min^{-1}$. The H_2 consumption was monitored by the TCD. Temperature-programmed desorption experiments on ammonia (NH_3-TPD) were conducted on a Quantachrome Autosorb iQ-C-TCD-MS. Before the test, 100 mg of the catalyst was outgassed at 300 °C for 2 h under a He atmosphere, then saturated with high-purity anhydrous ammonia at 50 °C for 1 h and subsequently flushed at 50 °C for 1 h to remove physically adsorbed ammonium. Finally, the TPD experiment was carried out from 50 °C to 700 °C at a heating rate of 10 $°C\cdot min^{-1}$. The product gases were analyzed with a quadrupole mass spectrometer. NO adsorption and temperature-programmed desorption (NO-TPD) were measured by KM9106 Quintox online flue gas analyzer. 100 mg sample was pretreated under a N_2 atmosphere (100 mL/min) at 350 °C for 1 h, and then cooling to 50 °C, the sample was exposed to a gas mixture of 500 ppm NO in N_2 with a total flow rate of 200 mL/min for 1h. Then the sample was purged with N_2 at a flow rate of 200 mL/min for 1 h. Finally, TPD was carried out from 50 °C to 500 °C at the same flow rate of N_2 with a temperature ramp of 10 $°C\cdot min^{-1}$. X-ray photoelectron spectroscopy (XPS) spectra was recorded using a surface analysis system (Thermal ESCALAB 250) using Al Kα radiation, the binding energies were corrected by referencing the C 1s peak at 284.6 eV. In situ diffuse reflectance infrared Fourier transform spectroscopy (in situ DRIFTS) experiments were performed on a Bruker Tensor 27 spectrophotometer equipped with an MCT/A detector. Before to each experiment, the sample was heated to 350°C in a flow of argon (70 $mL\cdot min^{-1}$) for 1h and then cooled to 150°C. Background spectra were recorded in the Ar flow and automatically subtracted from the corresponding spectra. The spectrum was recorded using KBr pellet method in the range of 400-4000 cm^{-1} by accumulating 32 scans at a resolution of 4 cm^{-1}.

2.3. SCR Activity Measurements

The NH_3-SCR activity measurement was carried out in a fixed-bed quartz reactor with an internal diameter of 10 mm. Prior to each test, 300 mg of powdered sample was pressed into blocks and sieved with 20-60 mesh and then used. The constituent of mixed reactant gas was 500 ppm NO, 500 ppm NH_3, 3% O_2, and N_2 was used as balance gas, with a total flow rate of 200 mL/min, and gas hourly space velocity (GHSV) of 32 000 h^{-1}. The reaction was carried out from 100 to 350°C; all the catalysts were kept on stream at target temperature for 30 min. The concentration of the outlet gas was measured online by a FTIR spectrometer (Gasmet FTIR DX4000, Finland). The NO conversion was defined as

$$\text{NO conversion (\%)} = 100\% \times \left(1 - [NO_X]_{out} / [NO_X]_{in}\right)$$

$$N_2 \text{ selectivity (\%)} = \frac{1 - ([NO_2]_{out} + 2[N_2O]_{out})}{[NO]_{in} - [NH_3]_{in} - [NO]_{out} - [NH_3]_{out}} \times 100\%$$

Where [NOx] = [NO] + [NO_2], and the subscripts “in” and “out” indicate the inlet concentration and outlet concentration at steady state, respectively.

3. Results and Discussion

3.1 Characterizations of the catalysts

The ordered mesostructures and crystalline nature of $MnCo_2O_4$ were confirmed by low- and wide-angle XRD, respectively. As shown in Fig. 2A, all of the reflections could be indexed according to the standard data for $MnCo_2O_4$ (cubic, lattice parameter a = b= c = 8.269 Å, space group *Fd3m*, JCPDS card no. 23-1237), The characteristic reflections at 2θ = 18.55°, 30.54°, 36.00°, 37.64°, 43.76°, 54.34°, 57.91°, 63.62° and 75.30° corresponded to the (111), (220), (311), (222), (400), (422), (511), (440) and (533) phase structure of $MnCo_2O_4$, respectively. These diffraction peaks indicated the presence of spinel nanocrystallites.[37,38]The diffraction peaks of mesoporous $MnCo_2O_4$ were somewhat weaker and broader than those of $MnCo_2O_4$ nanoparticles, indicating a slightly lower overall nanostructural order (as frequently found for replicated materials) or smaller coherent scattering domains of mesoporous $MnCo_2O_4$. This was also confirmed by the N_2 physisorption isotherms which showed a less well-pronounced capillary condensation step. According to the Scherrer formula, the grain sizes of B-, 2D- and 3D-$MnCo_2O_4$ were 21.6 nm, 12.1 nm and 9.8 nm, respectively, which indicated that the mesoporous samples were composed of nanocrystalline subunits, consistent with the TEM observation. From Fig. 2B, the 2D-$MnCo_2O_4$ catalyst had three peaks (100), (110) and (220), corresponding to the structural (p6mm) characteristics, [39] the 3D-$MnCo_2O_4$ catalyst showed the (211) and (220) diffraction peaks, which were characteristic of a cubic (Ia3d) mesostructure, indicating a high degree of ordering of the mesoporous material.[40,41]

The N_2 adsorption-desorption isotherm and the pore size distribution patterns were shown in Fig.3 and Table 1. It could be found the surface area of 3D-$MnCo_2O_4$ was 92.9 m^2/g, and that of 2D-$MnCo_2O_4$ is 69.7 m^2/g, which were much larger than that of B-$MnCo_2O_4$ (7.4 m^2/g). The isotherms of B-$MnCo_2O_4$ showed the rare adsorption, and the BJH pore size distribution showed almost no apparent pore size distribution. The isotherms of 2D- and 3D-$MnCo_2O_4$ showed type Ⅲ curves with a H3-type hysteresis loop, which were not totally consistent with the replicates. The reason may be associated with the contribution from the lower structural order to some degree and interparticle voids, the crystallization and strong interaction of manganese and cobalt oxide species destructed a part of the pore walls in the annealing progress.[19,21,30,42] Moreover, the hysteresis ring of the 2D-$MnCo_2O_4$ was smaller than that of the 3D-$MnCo_2O_4$. Perhaps the 2D- and 3D- $MnCo_2O_4$ catalysts had different porous channel structures. The BJH pore size distributions of mesoporous materials showed that the 2D- and 3D-$MnCo_2O_4$ had the mesoporous diameters of maximum distribution, 3.5 nm and 3.2 nm, respectively. This further indicated that 2D- and 3D-$MnCo_2O_4$ were a prefect replica structure of their templates.

The mesoporous materials are further examined via TEM (Fig. 4). It was very clear that the both 3D-$MnCo_2O_4$ (Ia3d) and 2D-$MnCo_2O_4$ (p6mm) displayed arrays of high-ordered mesoporous structure, which was consistent with the low-angle XRD results. The representative HRTEM image of Fig. 4 D displayed distinct lattice fringes with an interplanar distance of 2.50 and 2.90 Å, corresponding to the spacings of (311) and (220) planes of $MnCo_2O_4$ crystals, respectively.[38] In addition, the chemical compositions of the $MnCo_2O_4$ are confirmed by energy-dispersive X-ray spectroscopy (EDX) analysis (Fig.4 F), which indicates an atomic Mn/Co ratio of 1:2.03, which perfectly agrees with the theoretical value.

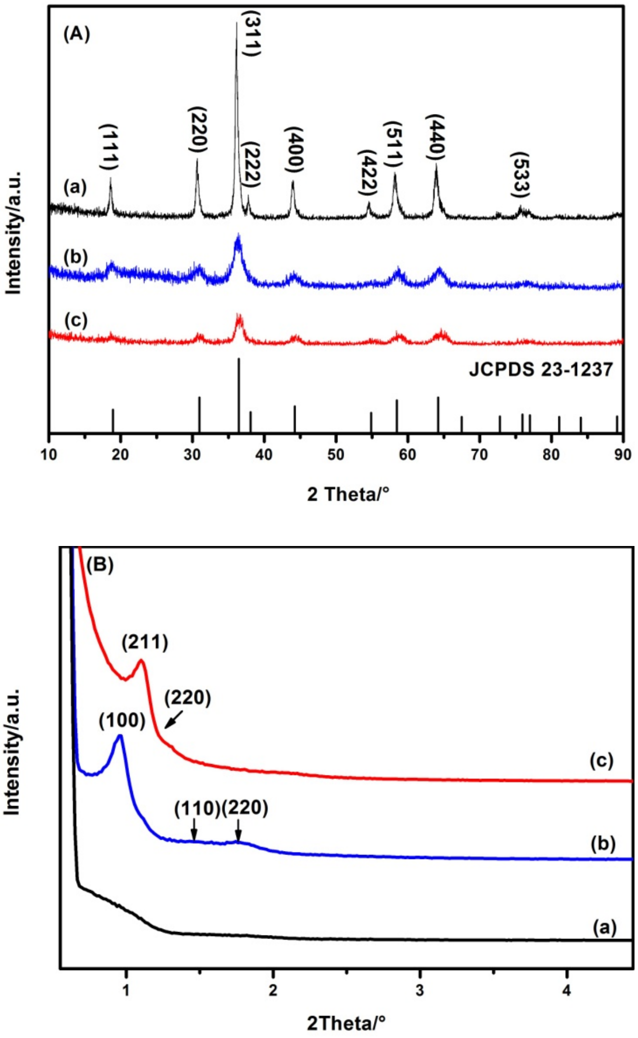

Fig.2. Wide-angle (A) and Low-angle XRD patterns (B) of replicas B-$MnCo_2O_4$ (a), 2D-$MnCo_2O_4$ (b), 3D-$MnCo_2O_4$ (c).

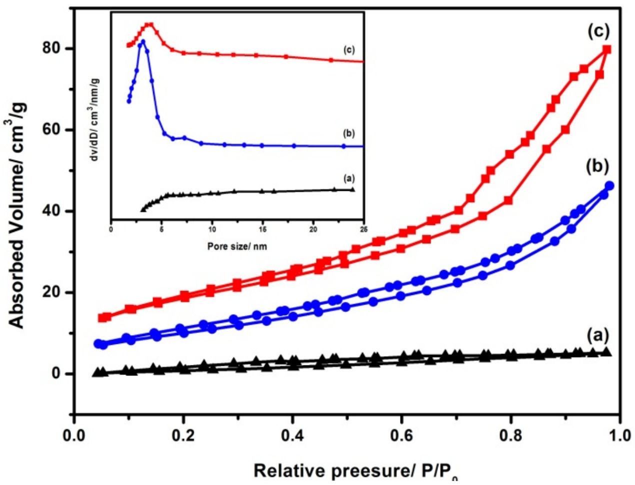

Fig.3. N_2 Adsorption-desorption isotherm and pore size distributions (inset) of (a) mesoporous 2D-$MnCo_2O_4$ and (b) mesoporous 3D-$MnCo_2O_4$

Table 1. Summary of textural parameters of the samples

sample	S_{BET}[m^2g^{-1}]	D_p [nm]	V_p [cm^3g^{-1}]
3D-$MnCo_2O_4$	92.9	3.5	0.17
2D-$MnCo_2O_4$	69.7	3.2	0.11
B-$MnCo_2O_4$	7.4	--	--

3.2. NH_3-TPD, H_2-TPR and NO-TPD

It was well noted that the adsorption of ammonia on the surface active sites of catalysts played a significant role in the NH_3-SCR reaction. The NH_3-TPD technique was used to investigate the surface acid amount and strength of the catalysts. Fig. 5A showed the NH_3-TPD profiles over the three catalysts. It could be seen that desorption of ammonia occurred over a wide temperature range, due to the presence of adsorbed ammonia species with different thermal stability. The peaks located at low temperature (166, 209 and 220 °C) could be ascribed to NH_4^+ bound to the Brønsted acid sites, while the peaks at high temperature (449 °C) were assigned to coordinated NH_3 originating from the Lewis acids.[20, 43, 44] However, there was the possibility of oxidation of strongly chemisorbed NH_3 with the lattice oxygen and a small amount of N_2O and NO were also desorbed, but the concentration was much lower than that of NH_3 in our study. In the whole temperature range, the 3D-$MnCo_2O_4$ catalyst showed the maximum NH_3 desorption amount. It was generally accepted that the area and position of desorption peaks were correlated with the acid amount and acid strength, respectively. As compared with B- and 2D-$MnCo_2O_4$, the strength of the Lewis acid sites on 3D-$MnCo_2O_4$ was much stronger. The ratios of NH_3 desorption amounts for B-$MnCo_2O_4$, 2D-$MnCo_2O_4$, and 3D-$MnCo_2O_4$ are approximately 1: 1.6: 4.7, respectively, this strong adsorption capacity of NH_3 could be associated with the strong interaction between manganese oxide and cobalt oxide species.[20] More importantly, the higher number of Lewis acid sites could be attributed to its larger specific surface area and characteristic of the ordered 3D porous structure, exhibiting a bimodal pore size distribution composed of small and large diameter pores, different from B- and 2D-$MnCo_2O_4$.[18,19,29]The difference in the strength and number of acid sites may result from their specific structural features, leading to the distinction of the catalytic performance.

The H_2-TPR measurements were used to evaluate the reducibility of the catalysts, and the obtained H_2-TPR profiles were illustrated in Fig. 5B. As shown, there were three reduction peaks (320, 650 and 794 °C) for B-$MnCo_2O_4$ and two reduction peaks (450 and 617 °C) for 2D-$MnCo_2O_4$. In the case of as for 3D-$MnCo_2O_4$, there are two peaks observed (ca. 421 and 619 °C). Previous studies had demonstrated that there were two H_2 consumption peaks at ca. 300 and 415 °C for Co_3O_4, ascribed to the stepwise reduction of $Co_3O_4 \rightarrow CoO \rightarrow Co^0$. It had also been reported that the profile of MnOx exhibited two reduction peaks at approximately 285 and 430 °C, belonging to the reduction of $MnO_2 \rightarrow Mn_3O_4 \rightarrow MnO$.[45] Based on these results, the peak at 320 °C in the bulk catalyst indicated that a part of Co^{3+} were reduced to Co^{2+}, but the spinel structure still remains.[20] The peaks at 421 °C and 450 °C could be the reduction of Mn^{3+} and Co^{3+}. The peaks at above 600 °C were ascribed to the stepwise reduction of $MnCo_2O_4$, involving the bulk oxygen species of cobalt and manganese oxides in mixed valences. Das et al.[46] reported the reduction of pure $(Co_{1-x}Mn_x)_3O_4$ phase at a temperature slightly above 600 °C. Therefore, it is reasonable to deduce that there is a strong interaction between manganese oxide and cobalt oxide species in $MnCo_2O_4$, especially for 3D-$MnCo_2O_4$. The presence of the strong interaction between manganese oxide and cobalt oxide species could play a synergistic role in the reducibility of the catalysts, leading to the enhancement of catalytic activity in the NH_3-SCR reaction. In addition, it should be pointed out that the area of the reduction peak had a direct relationship with the consumed content of H_2. It could be seen that 3D-$MnCo_2O_4$ exhibited the largest H_2 consumption among the three catalysts, indicating that 3D-$MnCo_2O_4$ exposed more reductive species, which should be beneficial to low temperature NH_3-SCR performance.

The adsorbed NO species on the surface of catalysts, especially those stored as surface nitrates, were suggested to play an important role in the reaction. So the NO desorption behaviors were investigated by means of TPD in order to evaluate the NO storage capacity of different catalysts, and the results were shown in Fig. 5C. As shown, two strong NO desorption peaks were observed at 155 and 334 °C on 3D-$MnCo_2O_4$, while only the first peak was found on 2D-$MnCo_2O_4$ and B-$MnCo_2O_4$. Usually, absorbed molecular NO firstly formed surface nitrosyls, and then oxidized to give rise to nitrite and nitrate species.[47] According to the previous reports,[48, 49] the first peak could be attributed to desorption of weakly adsorbed NO and/or decomposition of surface nitrites, while the peak at 334 °C could be ascribed to the strongly bound nitrate species, which were active reactive intermediates over these catalysts. In addition, it was noted that the intensity of NO desorption peak of 3D-$MnCo_2O_4$ was much larger than the others, attributing to the larger surface. The amount of NO desorbed from 3D-$MnCo_2O_4$, 2D-$MnCo_2O_4$, and

B-$MnCo_2O_4$, was 0.541, 0.174 and 0.117 mmol·g^{-1}, respectively.

3.3. X-ray photoelectron spectra (XPS)

In order to discover surface atomic compositions and oxidation states of the metal ions, the X-ray photoelectron spectra (XPS) was done and shown in Fig.6. Concerning the oxidation state of Co ions, four signals were detected in the Co 2p XPS spectra (Fig.6 A): two strong signals, at ~778.6 and ~793.2 eV, corresponding to the core levels of Co $2p_{3/2}$ and Co $2p_{1/2}$ with the spin-orbit doublet splitting of 15.4 eV and weak shakeup satellite peaks at ~787.7 and ~803.1 eV, respectively. Based on spin-orbit splitting of the main peaks and energy separation between the main peak and satellite peak, it was most likely that Co(II) and Co(III) coexist.[50-52] By using a Gaussian fitting method, the Co 2p spectrums were best fitted with two spin-orbit doublets characteristic of Co^{2+} and Co^{3+}, the ratio of Co^{2+}/Co^{3+} for the B-, 2D- and 3D-$MnCo_2O_4$ catalysts were 1.27, 1.04 and 0.99, respectively. Similarly, the Mn 2p XPS spectra (Fig. 6B) showed Mn $2p_{3/2}$ peak at ~640.1 eV and Mn $2p_{1/2}$ peak at ~651.7 eV, respectively. Among them, the peaks at ~640.2 and ~651.2 eV could be assigned to the presence of Mn(II), while other two peaks at ~641.5 and ~653.3 eV were characteristic of the Mn(III) cation,[49] the molar ratio of Mn^{2+} to Mn^{3+} for the B-, 2D- and 3D-$MnCo_2O_4$ catalysts was thus calculated to be 1.04, 1.00 and 2.16. The O1s peaks in Fig. 6C could be fitted into two peaks, the sub-bands at lower binding energy (530.4-530.7 eV) corresponded to the lattice oxygen O^{2-} (denoted as O_β), and the sub-bands at higher binding energy (532.2-532.8 eV) correspond to the chemisorbed oxygen (denoted as O_α), such as O_2^{2-} or O^- belonging to defect-oxide or hydroxyl-like group.[13-15] On one hand, the chemisorbed oxygen O_α had been reported to the most active oxygen in oxidation reactions due to its higher mobility, Besides, the high relative concentration ratio of $O_\alpha/(O_\alpha + O_\beta)$ on the surface of the catalyst could be correlated with the high NH_3-SCR activity.[20] The lattice ratio of O_α calculated by $O_\alpha/(O_\alpha + O_\beta)$ on the 3D-$MnCo_2O_4$ catalyst (52.7%) was much higher than 2D-$MnCo_2O_4$ (43.8%) and B-$MnCo_2O_4$ (37.3%), indicating that the morphological features could produce extra surface vacancies to activate oxygen and also more surface hydroxyls participating into the SCR reaction, which could facilitate to transform NO to NO_2, so the SCR reaction efficiency could be increased significantly.

3.4 Catalytic performance

The NH_3-SCR activities of different temperatures were shown in Fig.7 A. It could be found that the B-$MnCo_2O_4$ only maintained lower activity from 100 to 300 °C, with a highest conversion of 92.5 % at 250 °C. As for mesoporous $MnCo_2O_4$, the low temperature SCR activity was significantly enhanced with total NO conversion at 100 °C, 83% NO conversion for 2D-$MnCo_2O_4$ could be reached, and 98% NO conversion could be reached for 3D-$MnCo_2O_4$. The excellent results may be attributed to the high specific surface and rich mesoporous channels, which generated a lot of active sites. Furthermore, the 2D- $MnCo_2O_4$ exhibited two-dimensional straight channel, and mesopores were parallel to each other with super microporous, but these micropores didn't connect with the main mesopores. As a contrast, for 3D-$MnCo_2O_4$, the three dimensional cross channel connected with lots of interconnected holes. The small holes among the mesopores were formed by high temperature removal of the organic template and could not be immersed by metal salt precursor solution. Those interconnected networks and well-ordered mesopores could provide great mass transfer ability and more inner surface area for the catalytic reaction, which was in favor of the NH_3-SCR reaction. As for N_2 selectivity, 3D-$MnCo_2O_4$ exhibited higher selectivity than the others, which can be attributed to the excellent NH_3 oxidation ability. As shown in Fig. S3, the NH_3 oxidation ability of mesoporous $MnCo_2O_4$ was obviously higher than that of B-$MnCo_2O_4$, benefiting from the mesoporous structures and the large BET surface area. Besides, the N_2O concentration in NH_3 oxidation reaction over mesoporous $MnCo_2O_4$ were much lower than that over B-$MnCo_2O_4$, suggesting that mesoporous $MnCo_2O_4$ were better in the inhibition of NH_3 unselective oxidation, which was probably associated with the uniform distribution of active sites and synergistic role between manganese oxide and cobalt oxide species.[20]

Because the low temperature NH_3-SCR device was arranged behind the flue gas desulfurization device, the vapor content in the flue gas was close to its saturation vapor pressure, so the low temperature NH_3-SCR catalyst must also have the properties of high activity at low temperature and strong moisture resistance. The stability and H_2O resistance ability of the 3D-$MnCo_2O_4$ catalyst were shown in Fig.7 B. The NO conversion of the catalyst was kept at ca. 99% during a 60 h continuous running duration. After the addition of H_2O, the NO conversion decreased to 92% and then maintained at *ca.*96% for the next 18 h. After the shutting off of H_2O, the NO conversion returned to 100% rapidly, indicating that the activity of 3D-$MnCo_2O_4$ catalyst recovered. It was believed that the inhibition of H_2O was due to possibly due the competitive adsorption of H_2O and the slow deposition of ammonium nitrate onto catalyst surface. Combining with the NH_3-TPD analysis, a large number of acid sites over 3D-$MnCo_2O_4$ catalyst might preferentially absorb NH_3 other than H_2O, which also led to the excellent H_2O resistance ability. Therefore, the 3D-$MnCo_2O_4$ catalyst not only showed a wide operating temperature window, but also exhibited good structure stability and H_2O resistance, suggesting that the 3D-$MnCo_2O_4$ catalyst was a good candidate for low temperature NH_3-SCR reaction. In addition, the catalytic activity of the 3D-$MnCo_2O_4$ catalyst was severely inhibited after introducing 200 ppm SO_2 in the feed gas since MnOx could be sulfated and form stable sulfate species.[3, 43] Hence, the SO_2 resistant behavior needed further improvement in the future.

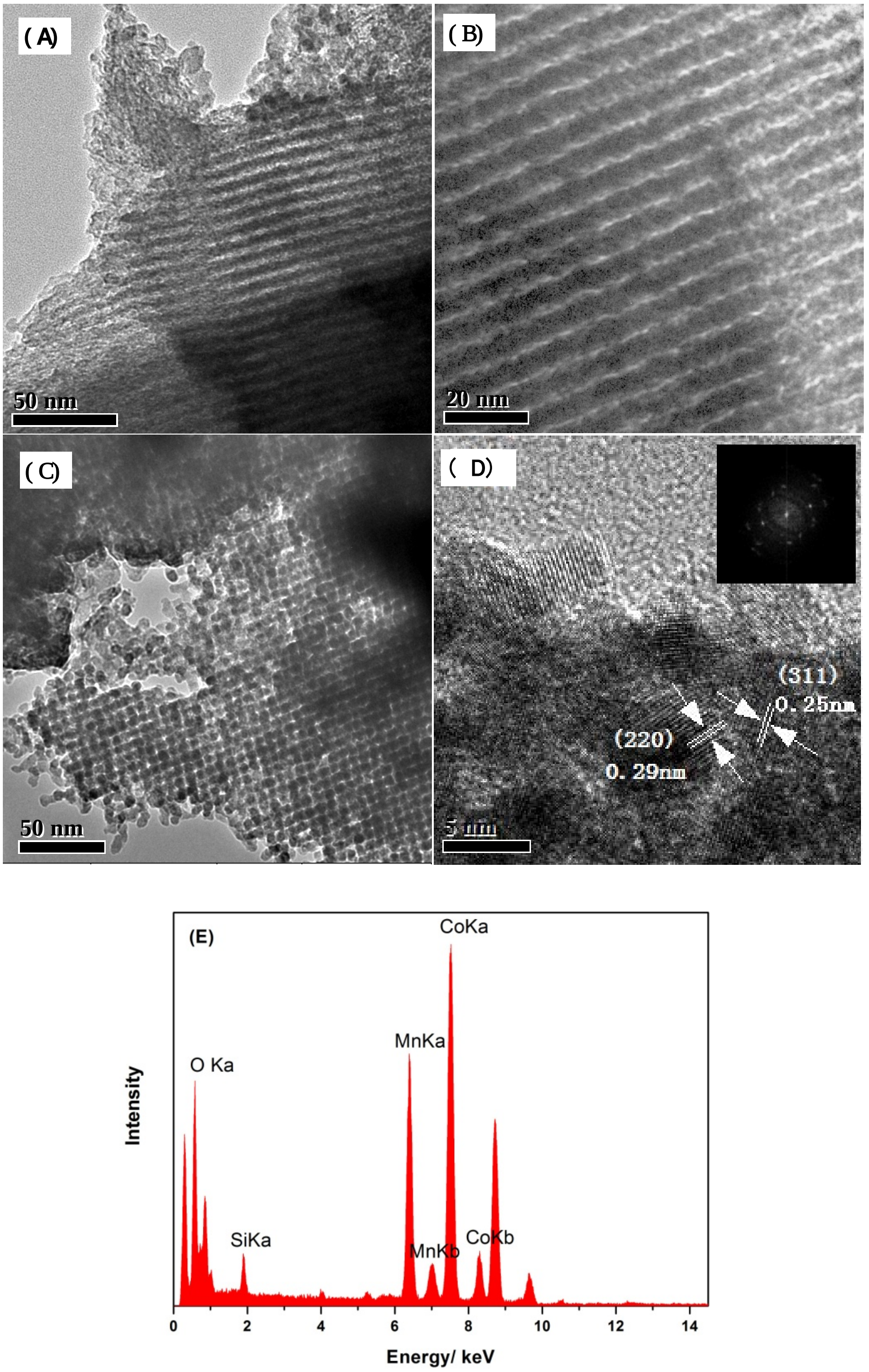

Fig. 4. TEM images of the different $MnCo_2O_4$ catalysts (A, B) 2D-$MnCo_2O_4$, (C) 3D-$MnCo_2O_4$. (D) HRTEM image of 3D-$MnCo_2O_4$ with the corresponding SAED pattern (the inset) (E) the corresponding EDX spectrum of 3D-$MnCo_2O_4$.

Nanoscale

Dynamic Article Links ►

Cite this: DOI: 10.1039/c0xx00000x

www.rsc.org/xxxxxx

ARTICLE TYPE

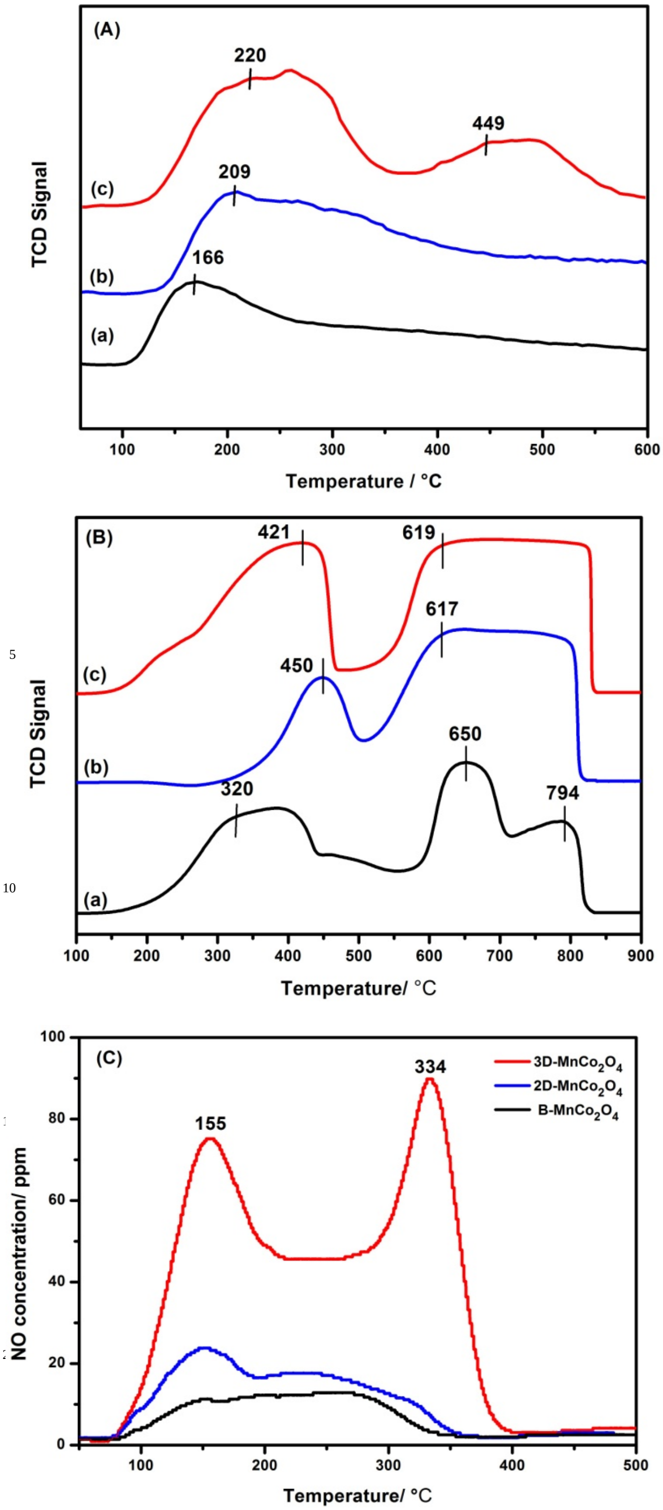

Fig. 5. NH_3-TPD patterns (A), H_2-TPR profiles (B) and NO-TPD profiles (C) of the different catalysts: (a) B-$MnCo_2O_4$, (b) 2D-$MnCo_2O_4$, (c) 3D-$MnCo_2O_4$.

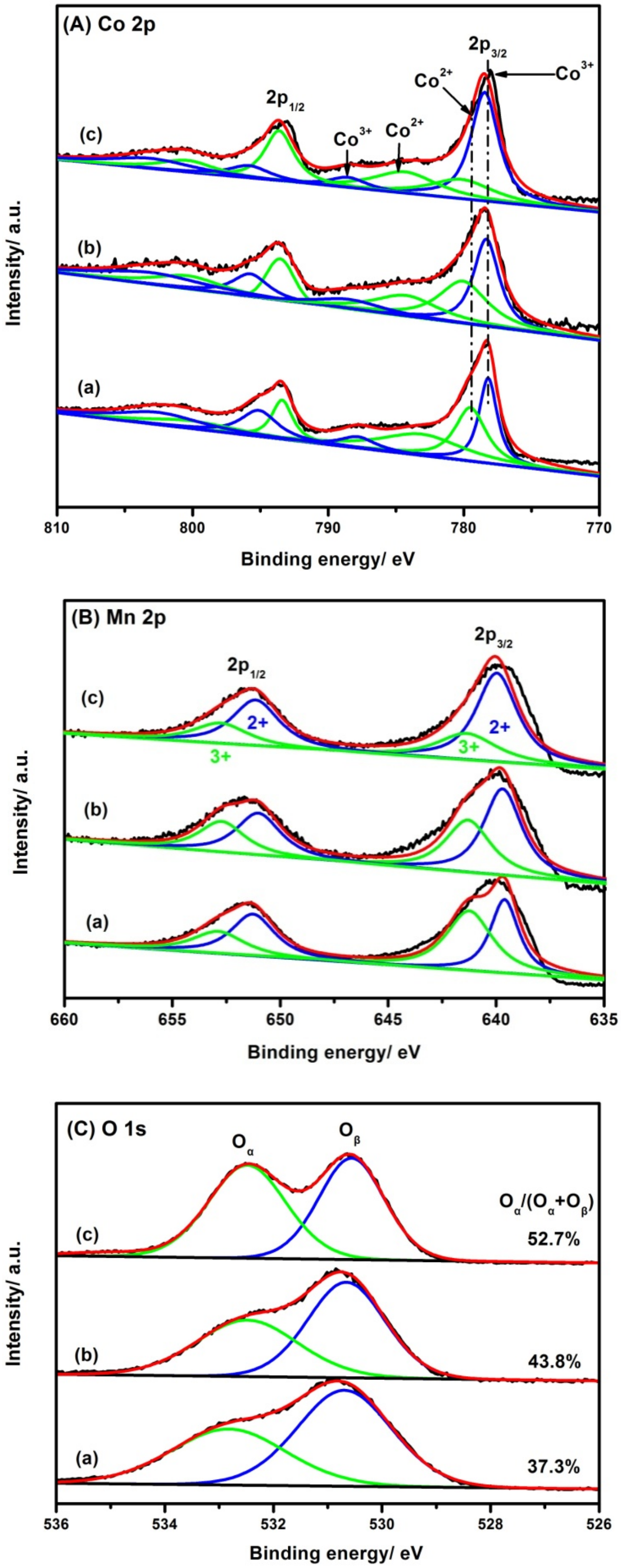

Fig.6. XPS spectra of Co 2p (A), Mn 2p (B) and O 1s (C). (a) B-$MnCo_2O_4$, (b) 2D-$MnCo_2O_4$, (c) 3D-$MnCo_2O_4$.

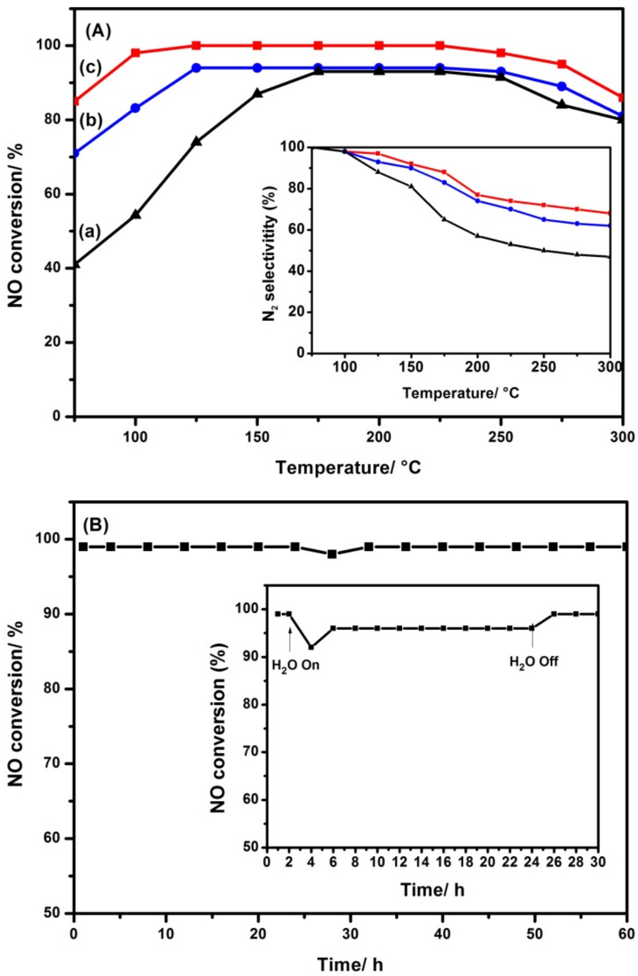

Fig. 7. (A)The NO conversion over different $MnCo_2O_4$; (B) Stability test and H_2O resistance study (inset) of the 3D- $MnCo_2O_4$ catalyst at 200 °C. Reaction conditions: 500 ppm NO, 500 ppm NH_3 , 3 vol% O_2, 6vol% H_2O, and N_2 as balance gas, GSHV =32,000 h^{-1} .

3.4. DRIFT Study-NH_3 adsorption and NO adsorption

As we all know, ammonia was mainly adsorbed onto Lewis and Brønsted acid sites to form coordinated NH_3 or NH_4^+ on the surface of metal oxides during SCR process, then the adsorbed nitric oxides can be reduced into form N_2 and H_2O. Therefore, it is very important to adjust acid sites on the SCR catalysts. Based on in situ DRIFTS spectra of NH_3 adsorption over different catalysts at 150 °C in Fig. 8A, the bands at 1200, 1603 and 1631 cm^{-1} are corresponded to coordinatively adsorbed NH_3 on Lewis acid sites, whereas the bands at 1457 cm^{-1} were attributed to asymmetric bending vibration of NH_4^+ species on Brønsted acid sites.[3, 52, 53] Meanwhile, the band at 1366 cm^{-1} was probably originated from oxidized species of the adsorbed ammonia species.[54] As shown in Fig. 8A, no obvious bands can be observed on the surface of B-$MnCo_2O_4$, probably due to its very small surface area. In contrast, two absorption peaks were visible slightly at 1457 and 1603 cm^{-1} and the peak at 1200 cm^{-1} was apparent on the surface of 2D-$MnCo_2O_4$. As to 3D-$MnCo_2O_4$, the Lewis acid sites (1200, 1603, and 1631 cm^{-1}) were obvious stronger. The ordered mesopores with narrow pore size distribution can provide valid space for the NH_3 diffusion and the large surface area offers more active sites.[20, 23] This was one key reason that mesoporous $MnCo_2O_4$ had higher adsorption capacity than the bulk catalyst. After NO + O_2 adsorption and N_2 purge at 150°C (Fig. 8B). A series of nitrate species absorption peaks are observed on the surfaces of bulk and mesoporous catalysts at 1624, 1552, 1528, 1309, 1280, and 1038 cm^{-1}. The band at 1624 cm^{-1} belongs to the bridge nitrate, the bands at 1552, 1528, 1309 and 1280 cm^{-1} are assigned to monodentate nitrate, [55, 56]and the band at 1343 and 1038 cm^{-1} are corresponded to bridge and monodentate nitrite, respectively.[53, 54] All the nitrate species absorbed on the mesoporous catalysts are similar to those on the bulk catalyst, except that the intensity of absorbance increased, especially the monodentate nitrate, the reactivity of which in SCR reaction was important. Therefore, the enhanced formation of monodentate nitrate was evidently responsible for the improvement of low temperature NH_3-SCR activity.

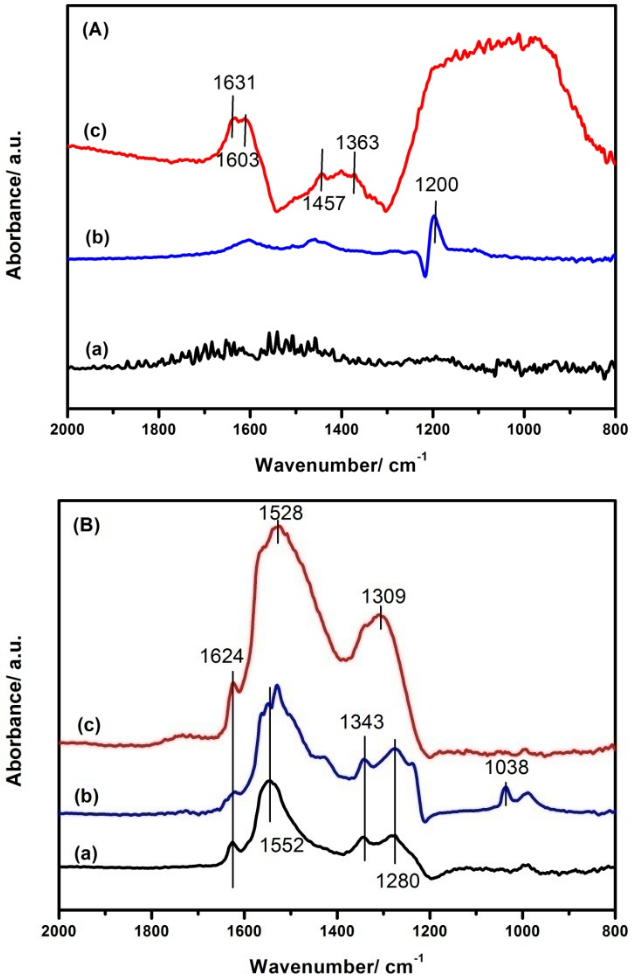

Fig.8. (A) NH_3 DRIFT adsorption and (B) NO + O_2 DRIFT adsorption over different catalysts at 150°C: (a) B-$MnCo_2O_4$, (b) 2D-$MnCo_2O_4$, (c) 3D-$MnCo_2O_4$.

4. Conclusions

In summary, highly ordered mesoporous $MnCo_2O_4$ are synthesized successfully by the nanocasting method, using of KIT-6 and SBA-15 as hard template, respectively. Among all of the catalysts, the 3D-$MnCo_2O_4$ templated from KIT-6 displays an enhanced NH_3-SCR activity, high N_2 selectivity, wide operating temperature window, high stability and water-resistance. The excellent catalytic performance of the catalyst can be attributed to the characteristic of ordered mesoporous structures as well as the strong interaction of manganese and cobalt oxide species, the larger acid amount and stronger acid strength. The feature of ordered mesoporous structures provides a larger surface area and more active sites to adsorb and activate reagents, resulting in the higher catalytic activity. In the future, the mesoporous $MnCo_2O_4$ catalyst can be considered as a promising candidate for the low-temperature NH_3-SCR reaction, and the mesoporous materials can be widely used in a lot of fields of environmental protection.

Acknowledgment

This study was financially supported by Natural Science Foundation of China (21377061 and 81270041), Asia Research Center in Nankai University (AS1326), Natural Science Foundation of Tianjin (12JCQNJC05800), and Key Technologies R&D Program of Tianjin (13ZCZDSF00300).

[a] *College of Environmental Science and Engineering, Nankai University, Tianjin300071, P. R. China; Fax: 022-23502756; Tel: 022-23502756; E-mail: sihuizhan@gmail.com*

† Electronic Supplementary Information (ESI) available: *Low-angle XRD patterns, Nitrogen physisorption isotherms of SBA-15 and KIT-6; NO conversion in separate NO oxidation reaction over different samples. NH_3 oxidation reaction over different samples.* Please see DOI: 10.1039/xxxxxxx/

References

1. C. Franch-Martí, C. Alonso-Escobar, J.L. Jorda, I. Peral, J. Hernández-Fenollosa, A. Corma, A.E. Palomares, F. Rey and G. Guilera, *J. Catal*., 2012, **295**, 22-30.
2. C. Fang, D. Zhang, L. Shi, R. Gao, H. Li, L. Ye and J. Zhang, *Catal. Sci. Technol*., 2013, **3** (3), 803-811.
3. F. Liu, K. Asakura, H. He, W. Shan, X. Shi and C. Zhang, *Appl. Catal. B*., 2011, **103** (3-4), 369-377.
4. J.O. Lee, Y.H. Song, M.S. Cha and S.J. Kim, *Ind. Eng. Chem. Res*., 2007, **46**, 5570-5575.
5. Y. Li, J.H. Peng, X. Huang, X. Li, W.K. Su, X.X. Sun, D.Z. Wang and J.M. Hao, Environ. Sci. Technol., 2014, **48**, 4515-4520.
6. Q. Li, H.S. Yang, F.M. Qiu and X.B. Zhang, J. Hazard. Mater., 2011, **192**, 915-921.
7. J. Li, H. Chang, L. Ma, J. Hao and R.T. Yang, Catal. Today, 2011, **175**, 147-156.
8. M.S. Maqbool, A.K. Pullura and H. P. Ha, Appl. Catal. B, 2014, **152-153**, 28-37.
9. Y. Peng, J. Li, W. Shi, J. Xu and J. Hao, Environ. Sci. Technol., 2012, **46**, 12623-12629.
10. W. Tian, H. Yang, X. Fan and X. Zhang, *J. Hazard. Mater*., 2011, **188**, 105-109.
11. L. Zhang, D.Zhang, J. Zhang, S. Cai, C. Fang, L. Huang, H. Li, R. Gao and L. Shi, *Nanoscale*, 2013, **5**, 9821-9829.
12. S. Cai, D. Zhang, L. Shi, J. Xu, L. Zhang, L. Huang, H. Li and J. Zhang, *Nanoscale*, 2014, **6**, 7346-7353.
13. P. Maitarad, D. Zhang, R. Gao, L. Shi, H. Li, L. Huang, T. Rungrotmongkol and J. Zhang, *J. Phys. Chem. C*, 2013, **117**, 9999-10006.
14. L. Zhang, D.Zhang, J. Zhang, S. Cai, C. Fang, L. Huang, H. Li, R. Gao and L. Shi, *Nanoscale*, 2013, **5**, 9821-9829.
15. Y. Wan, W. Zhao, Y.Tang, L. Li, H. Wang, Y. Cui, J. Gu, Y.Li, and J. Shi, *Appl. Catal. B*, 2014, **148-149**, 114-122.
16. C. Yu, G. Li, S. Kumar, Y. Kai and R. Jin, *Adv. Mater.*, 2014, **26**, 892-898.
17. G. Li and R. Jin, *Accounts Chem. Res.*, 2013, **46**, 1749-1758.
18. C. Ma, D. Wang, W. Xue, B. Dou, H. Wang and Z. Hao, *Environ. Sci. Technol*., 2011, **45**, 3628-3634.
19. C. Ma, Z. Mu,J. Li, Y. Jin, J. Cheng, G.Q. Lu, Z.P. Hao and S. Z. Qiao, *J. Am. Chem. Soc*., 2010, **132**, 2608-2613.
20. L. Zhang, L. Shi, L. Huang, J. Zhang, R. Gao and D. Zhang, *ACS Catal*., 2014, **4**, 1753-1763.
21. F. Jiao, A.H. Hill, A. Harrison, A. Berko, A.V. Chadwick and P.G. Bruce, *J. Am. Chem. Soc*., 2008, **130**, 5262–5266.
22. Y. Zhang, X.C. Zhao, Y. Wang, L. Zhou, J. Zhang, J. Wang, A. Wang, T. Zhang, *J. Mater. Chem. A*, 2013, **1**, 3724-3732.
23. Y. Ren, Z. Ma and P.G. Bruce, *Chem. Soc. Rev*., 2012, **41**, 4909-4927.
24. Q.S. Huo, D.I. Margolese, U. Ciesla, P.Y. Feng, T.E. Gier, P. Sieger, R. Leon, P.M. Petroff, F.Schuth and G. D. Stucky, *Nature*, 1994, **368**, 317-321.
25. D.M. Antonelli, A. Nakahira and J.Y. Ying, *Inorg. Chem*., 1996, **35**, 3126-3136.
26. A. Sayari and P. Liu, *Microporous Mater*., 1997, **12**, 149-177.
27. D.E. De Vos, M. Dams, B.F. Sels and P.A. Jacobs, *Chem. Rev*., 2002, **102**, 3615-3640.
28. J.D. Soler-Illia, C. Sanchez, B. Lebeau and J. Patarin, *Chem. Rev*., 2002, **102**, 4093-4138.
29. F. Jiao, H. Frei, *Angew. Chem. Int. Ed.,* 2009, **48**, 1841-1844.
30. B. Bai, H. Arandiyan and J. Li, *Appl. Catal. B*, 2013, **142-143**, 677-683.
31. H. Yen, Y. Seo, S. Kaliaguine and F. Kleitz, *Angew. Chem. Int. Ed*., 2012, **51**, 12032-12305.
32. H. Yen, Y. Seo, R. Guillet-Nicolas, S. Kaliaguine and F. Kleitz, *Chem. Commun*., 2011, **47**, 10473-10475.
33. Y. Xia, H. Dai, H. Jiang, J. Deng, H. He and C. Au, *Environ. Sci. Technol*., 2009, **43**, 8355-8360.
34. D. Zhao, J. Feng, Q. Huo, N. Melosh, G.H. Fredrickson, B.F. Chmelka and G.D. Stucky, *Science*, 1998, **279,** 548-552.
35. F. Kleitz, S.H. Choi and R. Ryoo. *Chem. Commun*., 2003, 2136-2137.
36. J.C. Groen, L.A.A. Peffer and J.P. Ramirez, *Microporous Mesoporous Mater*., 2003, **60**, 1-17.
37. L. Yu, L. Zhang, H.B. Wu, G. Zhang and X.W. Lou, *Energy Environ. Sci*., 2013, **6**, 2664-2671.
38. C. Fu, G. Li, D. Luo, X. Huang, J. Zheng and L. Li, *ACS. Appl. Mater. Interfaces*, 2014, **6,** 2439-2449.
39. T. Waitz, T. Wagner, T. Sauerwald, C.D. Kohl and M. Tiemann, *Adv. Funct. Mater*., 2009, **19**, 653-661.
40. J.Y. Luo, J.J. Zhang and Y.Y. Xia, *Chem. Mater*., 2006, **18**, 5618-5623.
41. K. Jiao, B. Zhang, B. Yue, Y. Ren, S. Liu, S. Yan, C. Dickinson, W. Zhou and H. He. *Chem. Commun*., 2005, 5618-5620.
42. F. Jiao, A. Harrison, J.C. Jumas, A.V. Chadwick, W. Kockelmann and P.G. Bruce, *J. Am. Chem. Soc*. 2006, **128**, 5468-5474.
43. F. Liu, H. He, C. Zhang, W. Shan and X. Shi, *Catal. Today*, 2011, **175**, 18-25.

44 S. Roy, B. Viswanath, M.S. Hegde and G.J. Madras, *J. Phys. Chem. C*, 2008, **112**, 6002-6012.

45 C. Shi, Y. Wang, A. Zhu, B. Chen and C. Au, Catal. Commun., 2012, 28, 18-22.

46 D. Das, G. Ravichandran and D.K. Chakrabarty, *Appl. Catal. A*, 1995, **131**, 335-345.

47 B. Meng, Z. Zhao, X. Wang, J. Liang, J. Qiu, *Appl. Catal. B*, 2013, **129**, 491-500.

48 X. Wu, F. Lin, H. Xu and D. Weng, *Appl. Catal. B*, 2010, **96**, 101-109.

49 W.S. Kijlstra, D.S. Brands, E.K. Poels and A. Bliek, *J. Catal.*, 1997, **171**, 208-218.

50 B.J. Tan, K.J. Klabunde and P.M.A. Sherwood, *J. Am. Chem. Soc.*, 1991, **113**, 855-861.

51 J. Li, S. Xiong, X. Li and Y. Qian, *Nanoscale,* 2013, **5**, 2045-2054.

52 M.A. Langell, M.D. Anderson, G.A. Carson, L. Peng and S. Smith, *Phys. Rev. B*, 1999, **59**, 4791-4798.

53 Y. Liu, T. Gu, X. Weng, Y. Wang, Z. Wu and H. Wang, *J. Phys. Chem. C*, 2012, **116**, 16582-16592.

54 L. Chen, J. Li and M. Ge, *J. Phys. Chem. C*, 2009, **113**, 21177-21184.

55 A. Karami, V. Salehi, *J. Catal.*, 2012, **292**, 32-43.

56 C. Liu, L. Chen, J. Li, L. Ma, H. Arandiyan, Y. Du, J. Xu and J. Hao, *Environ. Sci. Technol.*, 2012, **46**, 6182-6189.